



Project no.043386

TRIGS

TRIGGERING INSTABILITIES IN MATERIALS AND GEOSYSTEMS

Sixth Framework Programme (FP6) - STREP

**New and Emerging Science and Technology (NEST)
Pathfinder Initiative**

Deliverable n. 5.5.2 Deliverable title: Report on scale effect and triggering in slope instability, from snow to rock and soil and in earthquakes.

Due date of deliverable: 31 December 2009

Actual submission date: 26 January 2010

Start date of project: 1 January 2007

Duration: 3 years

Organisation name of lead contractor for this deliverable: INGV

Diffusion Level: PU

Triggering in slope instabilities

Séchilienne Landslide, in the french Alps, provides an excellent opportunity to investigate the mechanisms responsible for the triggering of slope instabilities. The seismic monitoring of this rockslide has given a catalog of several thousand events, associated with rockfalls debris flows, and micro-earthquakes. Seismic monitoring offers an accurate estimation of the time of each event, in contrast with most landslide catalogs, where events are detected based on field observations or aerial images. This allows to investigate the time delay between a perturbation and the triggering of instabilities. The displacement is also monitored since 1996, with accurate and continuous measurements.

In order to study the correlation between rainfall and rockfalls at Séchilienne, we have estimated the cross-correlation function between the rate of rockfalls and the precipitations. This function can be interpreted as the average precipitation as a function of time before and after a rockfall occurrence. This method allows the comparison between rockfall occurrence and previous rainfall. It is useful to quantify the correlation and to estimate the time delay between precipitations and triggered rockfalls. Results are shown in Figure 1. The cross-correlation displays a maximum value of 0.27 for a time delay of about 30 minutes between precipitations and rockfall activity. The peak amplitude is much larger than the average value, indicating that the correlation is weak but significant. The cross-correlation function is asymmetric; it is wider for positive times (corresponding to events triggered by rainfall) than for positive times. This shows that rockfalls are not only sensitive to instantaneous rain, but also to previous rainfall, due to water infiltration or snow melting. Rockfalls may also trigger future events, thus increasing the duration of rockfall crisis after the end of the rainfall episode. These results have been published in [Helmstetter and Garambois, 2010].

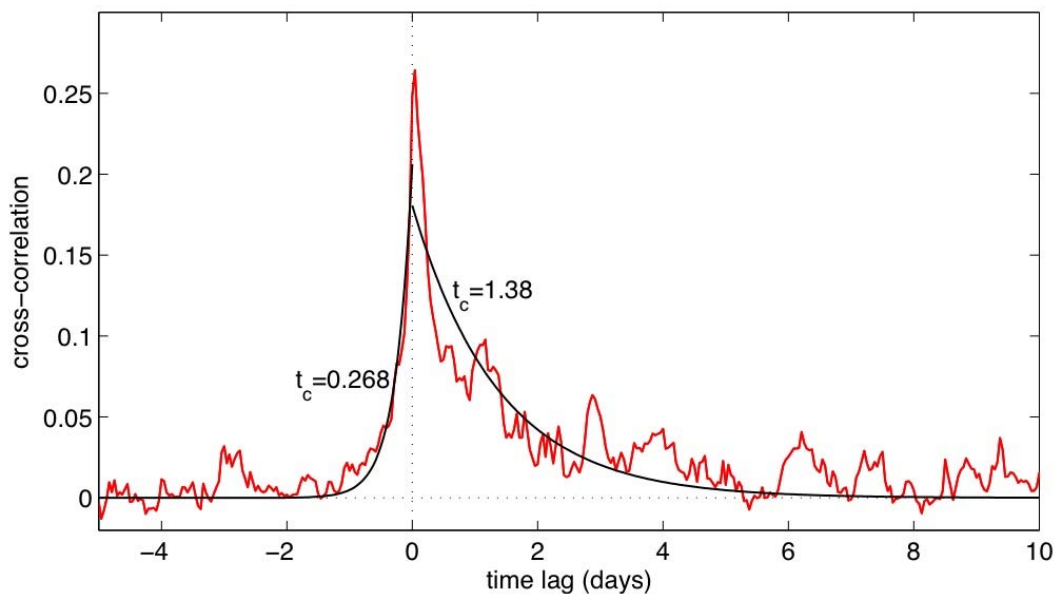


Fig 1: Cross-correlation function of the number of rockfalls per hour and precipitations.

In order to account for the influence of past precipitations on rockfall activity, we've applied the Antecedent Rainfall model [Crozier et al., 1980]. The cumulated rain is defined as the sum of hourly precipitations over all previous days, weighted by a function which decays exponentially with time. The relaxation time is estimated to be 0.24 day, by maximizing the correlation between

the cumulated rain and the number of rockfalls per hour. Using this model increases substantially the correlation between precipitations and rockfall activity. The results are shown in Figure 2. Rockfall activity increases linearly with precipitations, without any visible cut-off for small rainfall values. There is thus no evidence for a minimum threshold necessary for triggering landslides; 1 mm of rainfall seems to be enough for triggering rockfalls or micro-earthquakes.

We also analysed the influence of rainfall as a function of the size of rockfall or micro-earthquakes, and found that there is no qualitative difference between small and large events, the correlation between precipitation and rockfall or micro-seismicity does not depend on amplitude. Although rockfall occurrence increases with rainfall, only a weak proportion of rockfall events have occurred during the largest rain episodes. Indeed, only 2% of events have occurred when precipitation was larger than 1 cm/hr (see Figure 2c). Thus the probability of a moderate rockfall being triggered by a large rainfall is very small, because the probability of rockfall occurrence increases more slowly with the rainfall intensity than the decrease of the rainfall distribution.

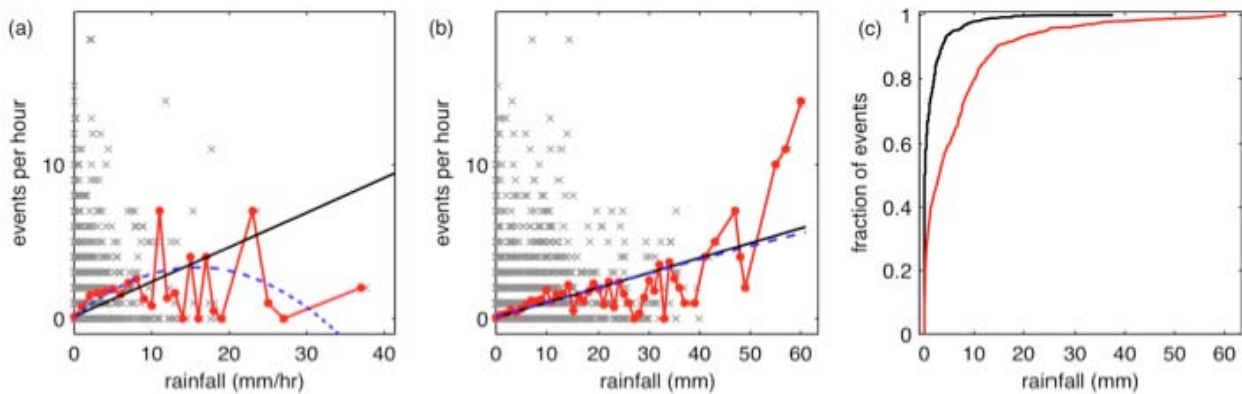


Fig 2: Number of rockfalls per hour as a function of (a) hourly precipitations and (b) cumulated precipitations (crosses). The solid line is a linear fit of hourly values, and the dashed line is a fit by a second-order polynomial. Red dots represent the average value of rockfall rate, obtained by binning the rainfall data with a bin width of 1 mm. (c) Fraction of events that have occurred for precipitations smaller than a given value, as a function of this threshold. Black line is for hourly precipitations, and red line is using cumulated precipitations.

Rain also induces strong accelerations of the rockslide movement, which also start quasi instantaneously, and last for about one month (see Figure 3). The displacement rate is delayed by a few days relative to rockfall activity, and decreases more slowly to its mean value, after about one month, compared to only 5 days for rockfall activity triggered by rainfall. This slow relaxation is likely due to inertial effects.

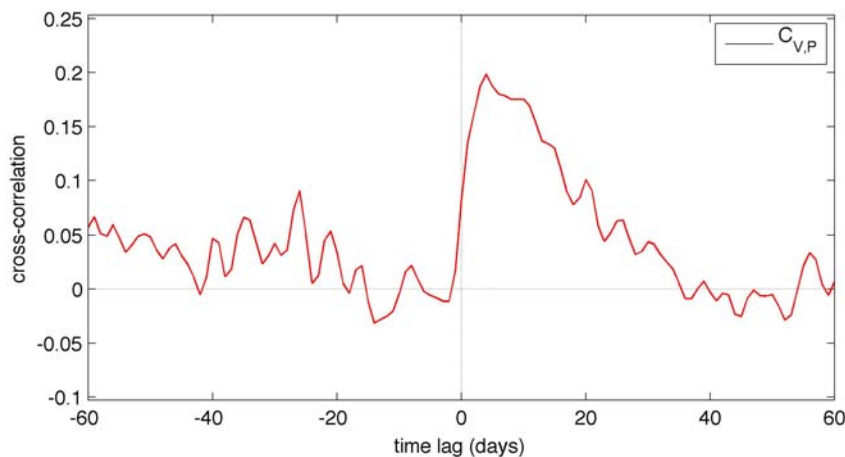


Fig 3: Cross-correlation between daily precipitations and displacement rate.

Scale effects in snow failure

Snow is a highly porous material of sintered ice crystals. The natural snow cover is a layered medium originating from deposition events. It is therefore highly anisotropic. Failure in snow leading to snow slab avalanche release forms near/along layer interfaces. Deformation due to gravity under normal conditions will cause bonds between grains to break, but also to sinter again in a closer packing (sintering dominates) and settlement of the snowpack is observed. On the other hand under conditions of fast loading or increased deformation due to an external perturbation, breaking of bonds dominates so that damage may accumulate resulting in a localized failure which eventually may reach a size sufficient for a self-propagating brittle fracture. This critical size has originally been estimated to be on the order of 0.1 m to 10 m (Schweizer et al., 2003), but is now believed to be – at least in the case of triggering by an external perturbation (near surface localized rapid loading) – about 0.5-1 m. This estimate is in agreement with the estimate by Bazant et al. (2003) and numerous fracture mechanical beam experiments confirm this order of magnitude (e.g. van Herwijnen et al., 2010). Also measurements on the impact of a skier in the snowpack indicate that the area that can be loaded is approximately $\leq 1 \text{ m}^2$ (Schweizer and Camponovo, 2001). The critical crack size is essential to understand the effect of spatial variations of snowpack properties on avalanche formation (Schweizer et al., 2008).

On the other hand, it is known that often only few force chains will carry most of the load within the fragile snow structure. Accordingly, the failure of one of these chains might light to catastrophic failure. This has been shown by simulation of the mechanical behaviour for small snow samples. The full 3-D representation of microstructure was used as input for a real microstructural (or specimen-specific) finite-element model (Schneebeli, 2004).

The discrepancy between the small scale experiments and the natural process during snow slab failure is likely due a lack of load sharing (as a consequence of the physical size) in the small scale experiments. Load sharing could be included in a simple fibre bundle model of snow failure (Reiweger et al., 2009). So far it has not clear, how results from small scale experiments/simulations that explicitly take into account the microstructure can be extrapolated to the snow slab release problem. Only for fracture experiments on snow beams of considerable size (0.5-1 m) the size effect has been shown and an approximate solution developed (Sigrist et al., 2005).

Acoustic emission triggering by fluids

An acoustic emission (AE) is defined as a transient elastic wave generated by the rapid release of energy within a material. In geological sciences studies of AE and seismology show a significant overlap. Both approaches deal with the radiation of elastic waves, although at different scales and frequencies.

The damage affecting a rock under load, in the brittle regime, involves the growth of microcracks from stress concentrators such as voids, inclusions and grain contacts, resulting in both inelastic strain and acoustic emissions. The acoustic signals that are spontaneously generated from the microcracking provide information about the size, location and deformation mechanisms of the events as well as properties of the medium through which the acoustic wave travel (e.g. velocity, attenuation and scattering).

Rock fracture and earthquake rupture are also processes obeying similar statistics for source dimensions over more than eight orders of magnitude (Hanks, 1992; Zang et al., 1998).

Frequency scaling offers the strongest argument to assess the equivalence of the physical processes between laboratory experiments and natural volcanic seismic signals. Experimental AE events have frequency of about 1-5 MHz for crack sizes between few tens to a few hundreds of mm. In natural earthquakes, dominant frequencies around 1-2 Hz are associated with fracture lengths of some hundreds meters to 1 km. Considering that dominant frequencies of earthquakes scale inversely with source dimension (Aki and Richards, 1980), one may write $d_1 \times f_1 = d_2 \times f_2$, where d_1 , d_2 and f_1 , f_2 are the dimension and frequency of laboratory (1) and nature (2), respectively. Comparing laboratory data with typical frequency (1-2 Hz) and size (1 km) of low frequency earthquakes, we obtain $d_1/d_2 = 5 \times 10^6$ and $f_2/f_1 = 2.5-5 \times 10^6$, which indicates excellent agreement between laboratory information and natural cases.

Recent laboratory experiments on Etna basalt (Benson et al., 2008) have permitted the generation of an extensive catalogue of acoustic emissions (AE) during two key experimental phases. Firstly, AE have been generated during triaxial compressional tests and formation of a complex fracture/damage zone. Secondly, AE have been triggered throughout rapid fluid decompression of the damage/shear zone after failure.

During the formation of the fault, waveforms show a distinctive, high frequency character (600-900 kHz), exhibiting a rapid onset (i.e. rapid acceleration) and relatively short duration (400 us). Conversely the 'triggered' events during the decompression stage exhibit a much lower frequency component (typically 80-100 kHz). The onset of these waveforms are highly emergent, and with longer duration, of the order of ms. In the following analysis we refer to these characteristic signals as high frequency (HF) and low frequency (LF) respectively.

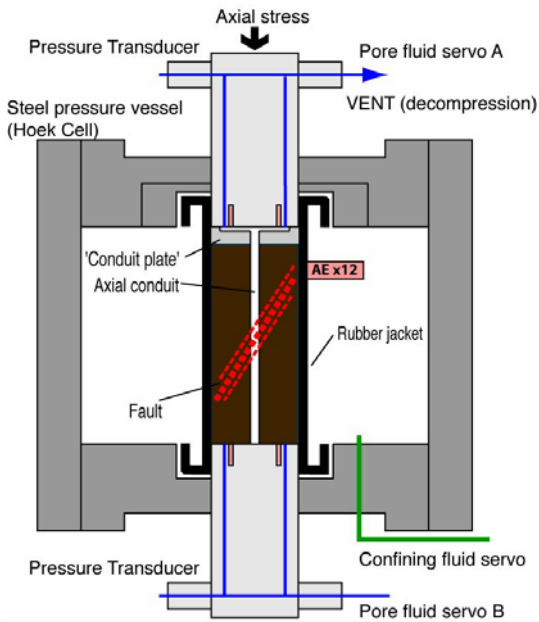


Figure 4. Scheme of the experimental setup (after Benson et al., 2008). Note that, for clarity, the precise locations of the 16 AE sensors (12 lateral and 4 axial) have been omitted.

The aim of the analysis consisted in statistically apply a classification method that is able to recognize different AE and their relation within each of the dynamic parts of the experiment. A key point is to classify the set of AE solely through spectral analysis, and then to test such classifications with other experimental information as occurrence time, load history, AE spatial location, etc. We look for an AE classification showing a consistent interpretation. If the interpretation is in agreement with the other experiment variables not involved, then we interpret this to have yielded two methodological useful results: we receive an independent confirmation of the reliability of classification method, and can elucidate the dynamical process.

Our classification is based on the application of factor analysis.

The data matrix is constituted by 280 FFT spectra calculated on AE waveforms in the frequency range 29 KHz - 493 KHz. The logarithmic amplitude of each spectrum is standardized in order to remove any effect due to AE magnitude. The range is then subdivided into 10 equal log intervals and mean amplitude for each interval is calculated.

The first factor shows a positive correlation of the low frequency range up to 70 kHz, while a negative correlation is found related to the highest frequency range (280-480 KHz). A moderate positive correlation occurs in the frequency interval 150-200 KHz (for the precise frequency interval see table 1). The second factor shows also a positive correlation in the frequency range 60-120 KHz interval, while a negative correlation is found in the 200-370 KHz interval. Third factor is negatively correlated in the 90-200 KHz interval and positively in the highest frequencies interval 370-500 KHz.

Through the factor scores, it is hence possible to represent data in a lower dimension factor space and to see the similar behaviour of each AE associated in specific factor space portion or clustered. Since the first factor is the most informative (figure 5), we show two scatter diagrams representing original AE spectra as defined respectively by I-II factors and I-III factors (Figures 7a, 7b).

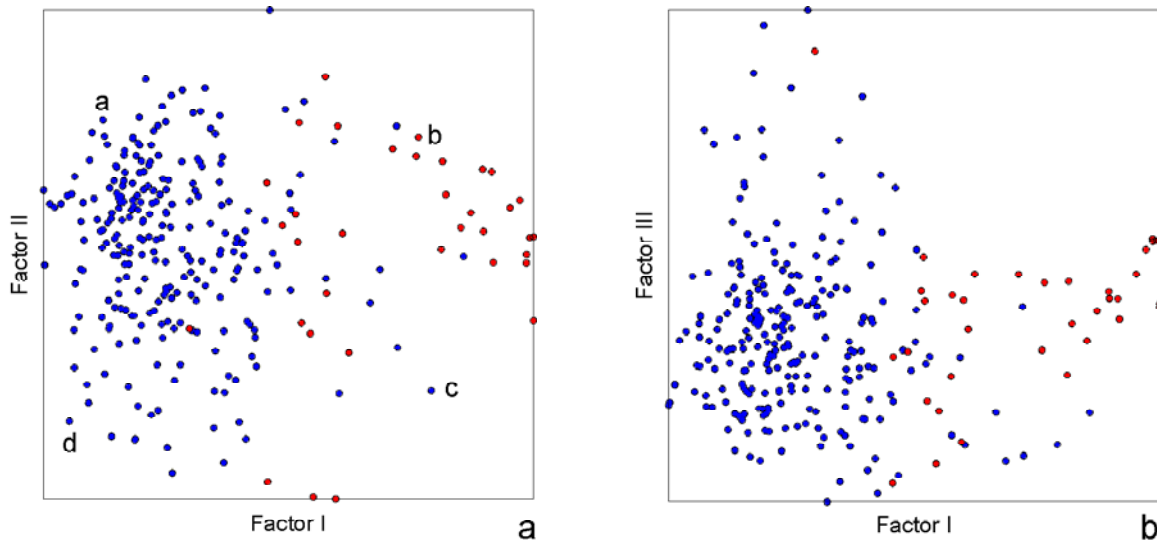


Figure 5. All 280 FFT spectra represented on the factor space following factor I with factor II scores (5a) and factor I with factor III scores (5b). In blue colour AE spectra recorded during deformation phase, in red those recorded during rapid decompression of the pore fluid. Four spectra (a,b,c,d) are marked (5a) in order to interpret their factor space position under their spectral content.

In Figure 5(a) and 7(b), all 280 AE samples are represented in the factor space. Each factor holds the frequency spectral content discussed above. By construction factors are orthogonal, which it means they have no correlation: in fact points are distributed with zero linear correlation between the two factors. In order to achieve a full understanding of the inter-factor relationship, we selected (a, b, c, d in figure 5a) four binned spectra, which represent the end terms in the factor space, i.e. the frequency ranges analyzed.

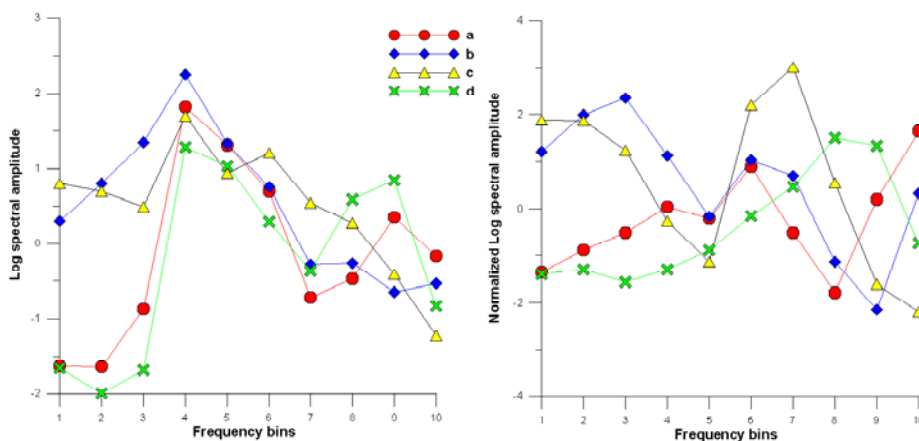


Figure 6. Four binned log amplitude spectra from AE sample data (a, b, c, d samples as referred into Figure 5a) as original values (left) and normalized values (right). Normalized spectra are represented to follow variables standardization applied to AE data matrix prior the extraction of eigenvalues and eigenvectors, as operated by factor analysis. See text for further details.

In detail, AE spectra a-d and c-b have similar factor I values while spectra a-b and c-d have similar factor II values. This similarity can be investigated by plotting the log of spectral amplitude vs. the frequency bins (Figure 6). AE spectra a-d and AE spectra c-b show correspondent amplitudes (bins 1,2,3,7,9) in spectral frequencies represented by factor I. AE spectra a-d hold low amplitudes in frequency bins 1,2,3,7 (positive correlation) and high amplitudes in bin 9 (negative correlation). AE

spectra c-b show an opposite behaviour. Analogue considerations apply for the factor II.

Factor analysis provides a quantitative tool to systematically discriminate AE events generated during deformation phase of the experiment (blue dots in Figure 5) from those recorded during rapid decompression of the pore fluid (red dots in Figure 5). High (HF) and low frequency (LF) events fill specific sectors in the factors space. In detail the LF events reflect the pure origin of fluid triggered events, due to the pore fluid flashing onto the damage/shear zone. No reactivation of cracks in terms of shearing/propagation of existing microfractures is triggered from the fluid propagation onto the fault plane, as no HF components are found from the factor analysis. HF shows a wider range of amplitudes involved. This can be explained from the fact that the energy and size of HF events increases over time as micron to mm scale cracks are involved in the early stage of deformation, followed by cm scale faults formation at the failure.

The most intriguing observation is given from the position of several events generated during deformation phase (where HF events only were believed to occur) in the factor space domain of the LF events (blue dots in Figure 5). This suggests that these events were generated from analogous mechanisms, which led to the formation of the LF, i.e. fluid migration onto the faults and triggering of the events. We interpret this behaviour due to the fact that during loading cracks open and shear. At the same time pressurized fluids rapidly transit into the crack surfaces and trigger same LF signals, similarly to those generated from pure fluid decompression in stage 2 (red dots in Figure 5). Taken together this emphasizes as factor analysis applied to a given AE data set can allow to highlight bulk AE patterns, that otherwise can not be easily seen by a pure visualization of single events.

Earthquake triggering

Earthquakes are the answer to tectonic load; stress is redistributed through the earthquakes, causing the aftershock sequence to develop in space and in time. Triggering of earthquakes may acts at several spatial and time scales. Short-range triggering (distance of the seismic fault size) is due by stress changes induced by the main-shock and related aftershocks in a recursive process. Marsan et al. (2000) investigated space-time relations of scale-invariance of seismicity. They pointed out that space and time should not be considered separately, but rather the spatial correlation structure is evolving in time. It is thus important to consider the spatial and temporal aspects of the seismic process simultaneously, in a combined way. In this work we apply a method of analysis, suitable to point processes and based on space-time correlations among earthquakes (Tosi et al., 2008). Like the previously cited authors, we do not separate seismicity into main and aftershocks. The aim was to study the behavior of seismic sequences in space and time. Seven different seismic catalogues have been analyzed: Greece, Japan, South California, Italy and Global CMT catalogue. The results show a statistical property of the different seismic catalogues that can be interpreted as an average behavior of seismic events following each earthquake. The spatial and fractal dimension measures the clustering respectively of hypocenters and time occurrences. The spatial analysis gives an insight of the extension of the seismic zone, while the temporal analysis shows the duration of the perturbation induced by a seismic event. In fact the result shows that after the occurrence of each event, there is a space-time domain inside which the subsequent events have temporally clustered occurrences (low time correlation dimension). These events are time correlated and are distinct from events occurring far away or after a long time interval, that are characterized by a random process (high time correlation dimension). Figure 7 shows that the overall clustering pattern is quite similar for all catalogues, suggesting an intrinsic physical process linked to earthquake occurrence. The blue domain, identifying low fractal dimension, has the greatest spatial extension at 10 days for

the global catalogue, while for regional ones it reaches maximum at around one month after the occurrence of the parent earthquake. During the following days, the clustering domain spatially shrinks, but it is still present after more than 8 years for all regional catalogues. The difference among clustering spatial extensions is probably linked to the strongest earthquake recorded in each catalogue, that is: $m=9.5$ for global CMT, $m=7.5$ for Greece, $m=8.3$ for Japan, $m=7.3$ for South California and $m=5.8$ for Italy. Our analysis indicates that the spatial influence range of each clustering sequence shrinks over time following a power law (Tosi et al., 2008). The long distances reached by the clustering sequence 10 days after the occurrence of the reference earthquake, suggests the presence of a long-range interaction.

Earthquake sequence is usually studied analyzing the event number per day and its decrease in time.

The power-law decrease is described by the Omori law or by its modified version: $n(t) = \frac{k}{(c+t)^p}$.

Where $n(t)$ is the number of earthquakes per day, t is time from the main shock, k reflects the seismic productivity and c is the "time offset" parameter; p modifies the decay rate and typically falls in the range 0.7–1.5. Traditionally the approach is to take a big event as a main shock. After having defined a suitable area, generally comprising the seismogenic fault, all events following the main shock are grouped and counted inside a proper time unit. We are interested to analyze the space-time relations of earthquakes triggered by a parent event. Assuming that every event can be a main shock of its own sequence, we count all succeeding events in function of both time and space distances. This space-time count is repeated for all events and the result is a stacked generalized count. It is worth to note that, taking into account different spatial distances, the number of event pairs at bigger distances increases according to the geometrical extension of the area embedding the events. To account for this effect the number of succeeding events is given normalized by the area of the circular annulus at a given distance. The result of the Omori count is given at three distances ranges, for all analyzed catalogues. Specifically these ranges are: 3-10km, 10-32km and 32-100km. In figure 8 the three space ranges are displayed respectively in blue (closest range), green (intermediate) and red (farthest) for all five catalogues. The closest range shows a quite similar behavior to the standard Omori law for a single main event in terms of c and p parameters. In fact the standard Omori count reflects the number of events decay at closest distances from the epicenter, as defined by the size of the seismic fault. Stacked approach is in agreement with the standard Omori law and allows a more stable statistical analysis, as required by the spatial subdivision. Results are in agreement with the standard Omori p values but more articulated. In fact the slope of the decay rate is small in the first time period after the main shock (first 10-20 days) before to reach typical Omori values. Behavior is influenced by spatial distance: p values are smaller increasing the distance from parent shock. After a period of hundreds of days the typical Omori p values disappear in favor of little or no decay.

An interesting point comes out from the comparison with the analysis of temporal fractal dimension as function of space and time. The temporal clustering caused by an event (figure 7) lasts for longer time in respect to the end of the Omori power law (figure 10) for the same distance range. This suggests a different definition of a seismic sequence, in dependence of the analyzed aspects: time, space and occurrence rate. In fact, while the rate decay pertains to the seismic activity increase due to sequence triggering, the temporal clustering takes occurrence disposition into account. Low fractal dimension indicates time clustering. When the seismic sequence is characterized by an increased seismicity is easily recognizable. On the other side, time clustering in periods of normal or slightly high background activity may indicate that the influence of the mainshock is still present. This influence reflects the persisting of triggering by parent event: the seismic activity, although at background rates, is not random, but is instead characterized by seismic shadows and clusters.

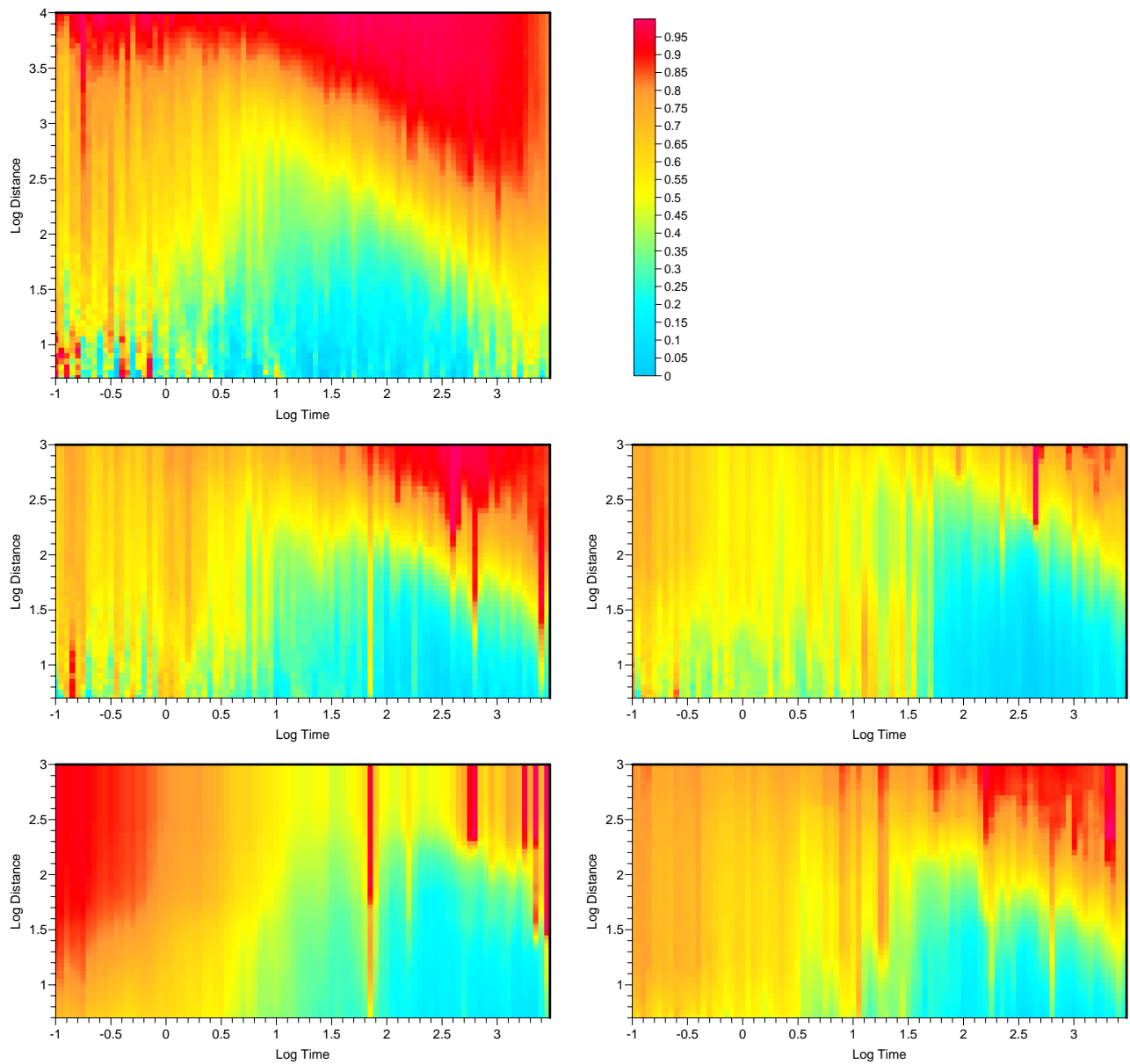


Figure 7. Local slopes of the of time correlation dimension. From top to down and left to right: Global CMT, Greece, Japan, South California and Italy catalogues

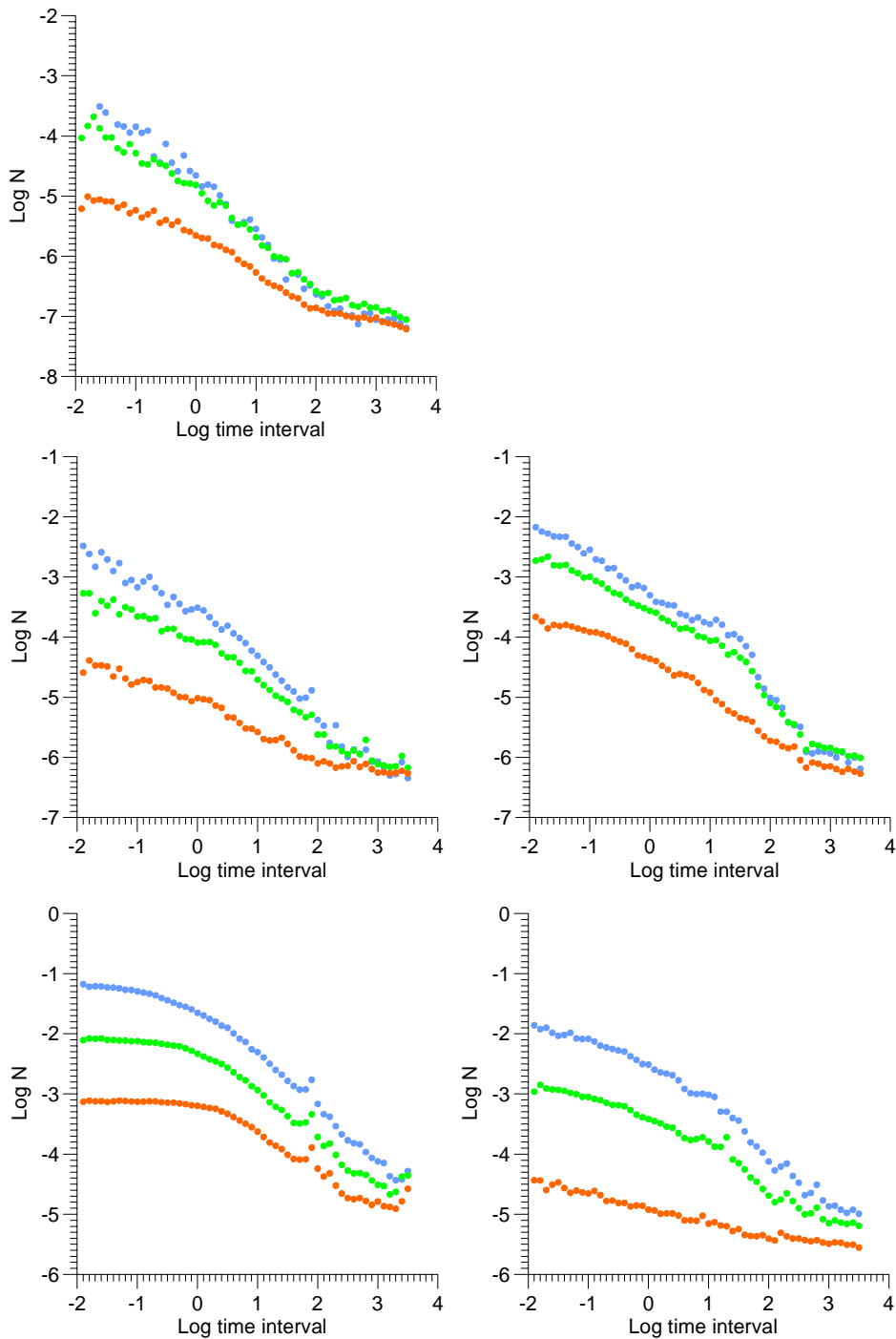


Figure 8. Stacked earthquake rate decay for near (blue), intermediate (green) and long (red) distances. From top to down and left to right: Global CMT, Greece, Japan, South California and Italy catalogues

References

Aki, K., and Richards, P.G., 1980, Quantitative Seismology: Theory and Methods, Freeman & co., San Francisco (USA). 932 p.

- Bazant, Z.P., Zi, G. and McClung, D., 2003. Size effect law and fracture mechanics of the triggering of dry snow slab avalanches. *J. Geophys. Res.*, 108(B2): 2119, doi:10.1029/2002JB001884.
- Benson P.M., Vinciguerra S., Meredith P. Young P., 2008, Laboratory Simulation of Volcano Seismicity, *Sciences*, 322, 249, doi: 10.1126/science. 1161927.
- Crozier, M. J., and R.J. Eyles, 1980, Assessing the probability of rapid mass movement. In *The New Zealand Institution of Engineers, Proceedings of Technical Groups (ed.)*, Proc. Third Australia, New Zealand Conference on Geomechanics, Wellington, 247-251.
- Hanks, T.C., 1992, Small earthquakes, tectonic forces: *Science*, v. 256, p. 1430-1432.
- Helmstetter, A. and S. Garambois, 2010, Seismic monitoring of S echilienne Rockslide (French Alps): analysis of seismic signals and their correlation with rainfalls, in press in *J. Geophys. Res.*
- Marsan, D., C.J. Bean, S. Steacy and J. McCloskey, 2000, Observation of diffusion processes in earthquake populations and implications for the predictability of seismicity systems, *J. Geophys. Res.*, 105, 28081-28094.
- Reiweger, I., Schweizer, J., Dual, J. and Herrmann, H.J., 2009. Modelling snow failure with a fiber bundle model. *J. Glaciol.*, 55(194): 997-1002.
- Schneebeli, M., 2004. Numerical simulation of elastic stress in the microstructure of snow. *Ann. Glaciol.*, 38: 339-342.
- Schweizer, J. and Camponovo, C., 2001. The skier's zone of influence in triggering slab avalanches. *Ann. Glaciol.*, 32: 314–320.
- Schweizer, J., Jamieson, J.B. and Schneebeli, M., 2003. Snow avalanche formation. *Rev. Geophys.*, 41(4): 1016, doi:10.1029/2002RG000123.
- Schweizer, J., Kronholm, K., Jamieson, J.B. and Birkeland, K.W., 2008. Review of spatial variability of snowpack properties and its importance for avalanche formation. *Cold Reg. Sci. Technol.*, 51(2-3): 253-272.
- Sigrist, C., Schweizer, J., Schindler, H.J. and Dual, J., 2005. On size and shape effects in snow fracture toughness measurements. *Cold Reg. Sci. Technol.*, 43(1-2): 24-35.
- Tosi P., De Rubeis V., Loreto V. and Pietronero L., 2008, Space-time correlation of earthquakes, *Geophys. J. Int.*, 173, 932-941, doi: 10.1111/j.1365-246X.2008.03770.x
- van Herwijnen, A., Schweizer, J. and Heierli, J., 2010. Measurement of the deformation field associated with fracture propagation in weak snowpack layers. *J. Geophys. Res.*: under review.
- Zang, A., Wagner, F. C., Stanchits, S., Janssen, C., and Dresen, G., 2000, Fracture process zone in granite, *J. Geophys. Res.* 105, 23651–23661.